Analyst

Accepted Manuscript

ROYAL SOCIETY OF CHEMISTRY

www.rsc.org/analyst

Analyst

PAPER

Ultrahigh-contrast and broadband on-chip refractive index sensor based on surface-plasmon-polariton interferometer

Received 00th January 20xx,
Accepted 00th January 20xx

DOI: 10.1039/x0xx00000x

www.rsc.org/analyst

Yujia Wang,[a,b] Jianjun Chen,*[a,b] Chengwei Sun,[a,b] Kexiu Rong,[a] Hongyun Li[a] and Qihuang Gong[a,b]

Using a double-slit structure fabricated on a gold film or a subwavelength (300 nm) plasmonic waveguide, high-contrast and broadband plasmonic sensors based on the interference of surface plasmon polaritons (SPPs) are experimentally demonstrated on chips. By adjusting the focused spot position of the p-polarized incident light on the double-slit structure to compensate the propagation loss of the SPPs, the interfering SPPs from the two slits have nearly equal intensities. As a result, nearly completely destructive interference can be experimentally achieved in a broad bandwidth (>200 nm), revealing the robust design and fabrication of the double-slit structure. More importantly, a high sensing figure of merit (FOM*) of >1×10^4 RIU^{-1} (refractive index unit), which is much greater than the previous experimental results, is obtained at the destructive wavelength because of the high contrast ratio (C=0.96). The high-contrast and broadband on-chip sensor fabricated on the subwavelength plasmonic waveguide may find important applications in the real-time and independent sensing of the particles and molecules.

Introduction

During the past several decades, we have witnessed a growing development in the field of biological and chemical sensing based on optics.[1-3] Optical sensors, a powerful detection and analysis tool, have been developed by using ring resonators,[4] waveguides,[5,6] and metallic structures based on surface plasmons (SPs).[7-37] Among the above techniques, the SP-based sensors that used metallic structures have attracted enormous attention in recent years because of the obvious advantages for high-density optical integration. SPs, the electromagnetically excited coherent charge oscillations at a metal-dielectric interface,[38] are strongly confined at the metal surface and have huge field enhancement effects. These attractive properties make the SPs extremely sensitive to the variations of the local refractive index, which is the basis for the localized surface plasmon resonance (LSPR) sensors[7-19] and surface plasmon resonance (SPR) sensors.[20-26] Many nanostructures based on LSPR have been proposed to achieve a good sensing performance, such as nanorods,[7,8] nanocubes,[9,10] nanostars,[11,12] nanoantennas,[13,14] double nanopillars,[15] and metamaterials.[16-18] Because the electromagnetic field of LSP decays very fast into the surrounding medium, LSPR-based sensors are more suitable for the detection of a single molecule.[19] SPR-based sensors,[2,3,20-26] of which the electromagnetic field has larger interaction areas and longer decay lengths than that of LSPRs, are more sensitive to the surrounding bulk medium. For the SPR-based sensors of high sensitivities (13800 nm/RIU) with using the prism and array structures,[25,26] their main drawback is the bulky device structures, which make them difficult to be integrated into chips. Moreover, conventional SPR or LSPR sensors must work at the resonant wavelengths to maintain the high sensitivities because the sensitivities will be considerably decreased when the response spectra (such as the absorption, scattering, and extinction spectra) of the particles and molecules being detected are far away from the resonant wavelengths.[7-27] Hence, these sensors can only work at a fixed wavelength or a very narrow wavelength bandwidth, which considerably limits their spectroscopic capabilities and practical applications in sensing.

Recently, surface-plasmon-polariton (SPP) interferometry has been proposed as a feasible way to overcome the bulky structures.[28-37] For the electromagnetic waves, the contrast ratio of the interference patterns and spectra is an important parameter, and it is also one of the key performance criterions of the sensor based on interference.[35] When the interfering contrast ratio reaches up to C=1, a very small deviation from the completely destructive interference (induced by the surrounding variations) can be detected, which can significantly increase the sensing resolution.[35] In the Mach-Zehnder Interferometric scheme,[28,29] there are three factors that limit the interfering contrast. They are the difference of SPP excitation efficiency by the slit on the upper and lower surfaces of the metal film, the different propagation losses of the two SPPs on both surfaces of the metal film, and the different scattering efficiencies of the SPPs at the slit. These three factors resulted in a reported contrast ratio of the interference that was only about C=0.25.[28] As for the slit-groove structures,[30-34] the intensities of the interfering beams can't be balanced because of the low SPP excitation efficiency of the groove, the large SPP propagation loss, and the low SPP scattering efficiency of the slit. Thus, the contrast ratio of the interference in the reported slit-grooves structure is only about C=0.3.[30] To obtain a high-contrast interferometric sensor, the hole-grating structure[35,36] and slit-grating[37] were proposed to

[a] State Key Laboratory for Mesoscopic Physics and Department of Physics, Peking University, Beijing 100871, China. E-mail: jjchern@pku.edu.cn
[b] Collaborative Innovation Center of Quantum Matter, Beijing, China.

increase the excitation efficiencies of the SPPs. The contrast ratio of the interference was increased to about C=0.87 at the resonant wavelength.[35] However, the grating structures are not suitable for the broadband spectral sensing due to the narrow-band (<50 nm) resonant SPP coupling of the gratings.[22,38,39] Moreover, precision designs and accurate fabrications are needed to realize the completely destructive interference in the narrow-band resonant spectra of the gratings. This also may be an important reason for that the contrast ratio of the interference is difficult to be increased experimentally in the previous sensors.[28-37]

In this letter, we demonstrate a high-contrast and broadband on-chip sensor based on the SPP interference in a metallic double-slit structure, which doesn't need precision designs and accurate fabrications. Due to the interference of the SPPs from the two slits, the interference spectrum of the SPPs on the metal surface exhibits oscillation behaviour. The broadband interference spectrum will be shifted when the refractive index of the surrounding medium is varied. In this configuration, only the propagation loss needs to be compensated to achieve a high contrast ratio of the interference. By adjusting the spot position of the p-polarized incident light, we experimentally achieve a high contrast ratio (C>0.9) of the interference spectrum in a broad bandwidth (>200 nm). As a result, a high figure of merit (FOM*) at the destructive wavelengths in a broad bandwidth is obtained. Moreover, the whole structure of the SPP sensor can be made more compact by fabricating the double-slit aperture structure on a subwavelength (300 nm) plasmonic waveguide.

Design and principle

The proposed double-slit interferometer structure is schematically shown in Fig. 1(a). The structure consists of two nano-slits fabricated on a 450-nm-thick gold film, which is evaporated onto a glass substrate with a 30-nm-thick titanium adhesion layer. The focused ion beam (FIB) technology is used to fabricate the two nano-slits with the widths of w_1 and w_2, and the slit spacing is about L=43.86 μm. The scanning electron microscope (SEM) image of the double-slit structure is shown in Fig. 1(b). To eliminate the wavelength dependence of the SPP coupling from the incident light, we fabricate two identical slits on the metal surface in the experiment. The measured slit width is about w_1=w_2=200 nm. When the p-polarized light (magnetic vector parallel to the slit) normally illuminates the structure from the back side, the SPPs can be excited by the two identical slits to propagate along the metal surface[40] and then interfere with each other, as shown in Fig. 1(a). The amplitudes of the incident magnetic field on the two slits are $|H_1|$ and $|H_2|$, respectively. To measure the interference spectrum of the SPPs, a decoupling grating with a period of about 660 nm is fabricated on the left side of the double-slit structure with a separation of about 10 μm, as shown in Fig. 1(b). In the practical applications, the on-chip detectors[41] can be integrated on the metal surface, so the decoupling grating is not necessary.

It is easy to obtain that the phase difference between the two interfering SPPs is determined by

$$\Phi = \frac{2\pi}{\lambda} n_{\mathrm{eff}} L + \varphi, \qquad (1)$$

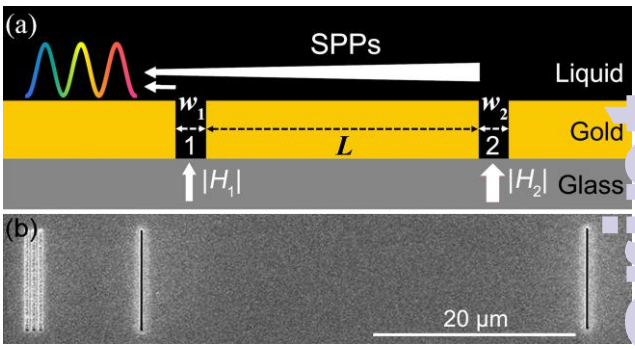

Fig. 1 (a) Schematic and geometrical parameters of the double-slit structure on a metal film. (b) SEM image of the experimental structure.

where λ is the wavelength of the incident light in the free space; φ is the phase brought by the SPPs passing through Slit 1; $n_{\mathrm{eff}}=[n_d^2\varepsilon_m/(n_d^2+\varepsilon_m)]^{1/2}$ is the effective refractive index of SPPs; n_d is the surrounding refractive index; and ε_m is the permittivity of the gold. The total interference intensity of the two SPPs can be written as

$$I \propto \left|1+a\exp(i\Phi)\right|^2 \propto 1+\frac{2a}{1+a^2}\cos(\Phi) = 1 + C\cdot\cos(\Phi), \qquad (2)$$

where, a is the amplitude ratio of the two interfering SPPs, and C=$2a/(1+a^2)$ is the interference contrast ratio. It is noted that the contrast ratio of C is only determined by the relative intensities of the two interference SPPs, so the decoupling grating will not change C even in a broad bandwidth. According to Eq. (2), constructive or destructive interference of the two SPPs from the two slits should occur when Φ equals even or odd multiples of π, and the period of the interference spectrum is

$$\Delta\lambda \approx \frac{\lambda^2}{n_{\mathrm{eff}} L}. \qquad (3)$$

From Eq. (3), we can obtain that the interference period is smaller when the slit spacing of L becomes larger.

Moreover, it can be obtained that the phase difference of Φ will change with the variations of the surrounding refractive index of n_d, which can lead to a shift of the interference spectrum. This is the mechanism of the refractive index sensor. The sensitivity in terms of the wavelength shift per refractive index unit (RIU) is determined by

$$S = \lim_{\Delta n\to 0}\frac{\lambda(n+\Delta n)-\lambda(n)}{\Delta n} = \frac{(\partial n_{\mathrm{eff}}/\partial n_d)\cdot(\lambda/n_{\mathrm{eff}})}{1-(\lambda/n_{\mathrm{eff}})\cdot(\partial n_{\mathrm{eff}}/\partial\varepsilon_m)\cdot(\partial\varepsilon_m/\partial\lambda)}. \qquad (4)$$

From Eq. (4), it can be concluded that the sensitivity of S has no relationship with the slit spacing of L. It should be pointed out that the sensitivity of S can only reveal the spectra shift when the refractive index of n_d is varied, but a small wavelength shift is difficult to be observed if the spectral bandwidth is very large.[9,19] To evaluate the performance of optical sensors more precisely, researchers introduced a figure of merit (FOM) that simultaneously considers the sensitivity and the sharpness of the spectral peak.[9] The FOM of the interferometric sensor can be derived from Eq. (3) and (4) to be

$$\mathrm{FOM} = \frac{S}{\delta\lambda} = \frac{2S}{\Delta\lambda} = \frac{(\partial n_{\mathrm{eff}}/\partial n_d)}{1-(\lambda/n_{\mathrm{eff}})\cdot(\partial n_{\mathrm{eff}}/\partial\varepsilon_m)\cdot(\partial\varepsilon_m/\partial\lambda)}\cdot\frac{2L}{\lambda}. \qquad (5)$$

To get a high FOM, we should choose a large slit spacing (L) based on Eq. (5). For the intensity-based sensing at a single wavelength,

another figure of merit, which can reveal how sharp the relative intensity change ($\Delta I/I_0$) induced by the refractive index change of Δn at a specific incident wavelength, can be derived from Eq. (2) to be[30]

$$\mathrm{FOM}^* = \lim_{\Delta n \to 0} \frac{\Delta I/I_0}{\Delta n} = \frac{C}{1-C}\frac{S}{\lambda} k_{spp} L \sin(\Phi), \quad (6)$$

where, $k_{spp}=2\pi n_{eff}/\lambda$ is the wave vector of the SPPs, and I_0 is initial intensity at the destructive interference as a reference or calibration (with a known concentration or refractive index). For the first part, $C/(1-C)$, of Eq. (6), its value increases greatly with C, especially as the interference contrast ratio approaches to C=1. For the second part, S/λ, it is a constant based on Eq. (4). The third part, $k_{spp}L$, linearly increases with the slit spacing of L. The last part, $\sin(\Phi)$, means that its value reaches to the maximum when Φ equals odd multiples of $\pi/2$ in the sensed medium. Therefore, high-contrast interference (C) and a long slit spacing (L) should be chosen to get high values of FOM*. However, because of the propagation loss of the SPPs on the metal surface, high-contrast interference is difficult to be achieved when the slit spacing becomes large. Hence, such a choice is subject to a trade-off between the contrast ratio of interference and the slit spacing. Here, we choose the slit spacing to be about 40 μm.

Results and discussion

High-contrast and broadband interference spectra in the double-slit structure

In the following, we test our proposal in both of the experiment and numerical simulation. First, we calculate the interference spectra with COMSOL Multiphysics, and the simulation data are shown in Fig. 2(a-c). Here, the refractive index of the known surrounding medium (water) is n_d=1.32165,[29] and the permittivity of gold as a function of λ is taken from the experiment results.[42] Because the propagation length of the SPPs increases with the wavelength, the completely destructive interference occurs at the long wavelengths when $|H_1|:|H_2|$=0.6:1, and the completely destructive interference occurs at the short wavelengths when $|H_1|:|H_2|$=0.2:1, as shown in Fig. 2(a, b). In order to obtain completely destructive interference in a broad bandwidth, $|H_1|:|H_2|$ should equal $\exp[-L/2L_{SPP}(\lambda)]$:1 to compensate the different propagation loss at different incident wavelengths, where $L_{SPP}(\lambda)$ is the propagation length of the SPPs at the incident wavelength of λ. The simulation data are shown in Fig. 2(c), where completely destructive interference is obtained in the whole wavelength band. The low intensity at the short wavelengths is attributed to the large propagation loss at these wavelengths.

In the experiment, we use a super-continuum white light source (Fianium) to illuminate the sample from the back side. The white light is first polarized to be a p-polarized light by a Glan-Taylor prism and then focused on the sample by a microscope objective (Mitutoyo 20×, NA=0.4). The SPPs excited by the two slits interfere with each other at the left side of the double-slit structure. To measure the interference spectra, the SPPs propagating along the metal surface are scattered by the grating and then are collected by another microscope objective (Mitutoyo 100×, NA=0.5), which is placed in air. The collected light is coupled to a fiber that connects a spectrograph (Andor). To compensate the propagation loss of the SPPs from Slit 2, the position of the incident light spot is adjusted to be close to Slit 2. Moreover, the radius of the focused spot on the sample is not a constant for different wavelengths because of the chromatism of the microscope objective. As a result, a broadband and high-contrast interference spectrum is obtained when the focused radius of the white light is about r≈30 μm and the focused position is just located at Slit 2, as shown in Fig. 2(d), which is similar to the simulation data in Fig. 2(c). Here, the bandwidth is more than 200 nm, and the contrast ratio is greater than C=0.9, which is greater than the previous results.[28-33,35,37] More importantly, since the nearly completely destructive interference can be realized in such a broad bandwidth (>200 nm), the precision design of the double-slit structure is not needed, and the sample fabrication is robust and easy. Simulations show that the deviations of slit width, film thickness, and waveguide dimensions have little influence on the sensor performance. It is found that the film thickness in the range of (100, 600) nm, the slit width in the range of (50, 800) nm, and waveguide dimensions of (50, 600) nm in widths and (50, 450) nm in heights are all OK for the sensors. This further reveals the robust realization of the nearly completely destructive interference in the double-slit structure, according well with the broadband property in Fig. 2(d).

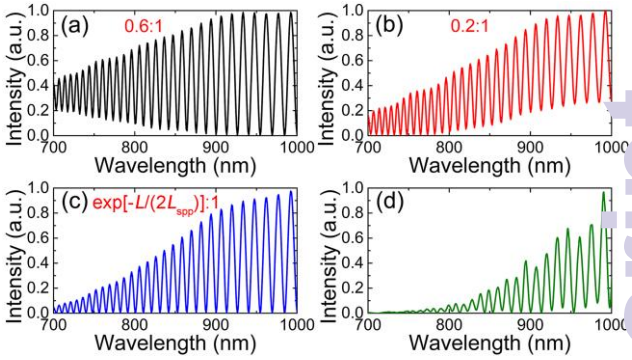

Fig. 2 Simulation data of the interference spectra in the double-slit structure as a) $|H_1|:|H_2|$=0.6:1, (b) $|H_1|:|H_2|$=0.2:1, and (c) $|H_1|:|H_2|=\exp[-L/(2L_{SPP})]$:1. (d) Experimental results of the interference spectra by adjusting the spot position of the incident light on the double-slit structure.

Refractive index sensing in the double-slit structure fabricated on the metal film

In order to verify the shift of interference spectra induced by the refractive index variations of the surrounding medium, we measured the interference spectra in 0%, 1%, 2%, 3%, and 4% NaCl-H_2O solutions, whose refractive indexes are 1.32165, 1.32326, 1.32500, 1.32674, 1.32848, respectively.[29] The measured results are shown in Fig. 3(a). Herein, the focused radius of the white light is about r≈30 μm, and the focused position is just located at Slit 2. To clearly observe the spectral shift induced by the refractive index variation, only the spectral range between 900 nm and 950 nm is chosen here. It is obviously that the interference spectra have a remarkable linear red-shift with increasing the refractive index of the liquids. Fig. 3(b) gives the simulation data, which agree well with the experimental results. The sensing performances obtained from the ex-

periment, simulation, and theory are listed in Table 1. It is observed that these results are in good agreements with each other. Moreover, it can be obtained from Fig. 2(d) that the interference contrast ratio is greater than C=0.9 in the wavelength range from 800 nm to 1000 nm because of the balanced intensities of the two interfering SPPs excited from the two slits. Such a high contrast is more favourable for intensity-based sensing.[19,30,35] For example, the destructive interference occurs when the surrounding medium is water, and the SPP intensity is close to zero [I_0≈0.016] at the incident light wavelength of λ≈913.6 nm. But the SPP intensity reaches I≈0.415 at the same incident light wavelength when the surrounding liquid becomes 4% NaCl-H_2O solution, as shown by the black dashed line in Fig. 3(a). Consequently, a little refractive index change (Δn=0.0068) will cause an extremely large relative intensity change [$\Delta I(\lambda)/I_0(\lambda) = (I-I_0)/I_0$×100% ≈ 2500%]. Therefore, we can measure the refractive index of a NaCl-H_2O solution with unknown concentrations by using $\Delta I/I_0$.

Based on the above analysis, the relative intensity changes ($\Delta I/I_0$) can be obtained by using the experimental interference spectra in 0%, 1%, 2%, 3%, and 4% NaCl-H_2O solutions. Fig. 3(c) is the spectra of the relative intensity changes ($\Delta I/I_0$) in the NaCl-H_2O solutions of different concentration. When the concentration of the NaCl-H_2O solutions increases from 0% to 4%, we can see that the relative intensity changes ($\Delta I/I_0$) reach peaks at the destructive wavelengths of λ=900.2 nm, λ=913.6 nm, λ=926.0 nm, and λ=939.4 nm. This proves that this plasmonic sensor can work at several wavelengths.

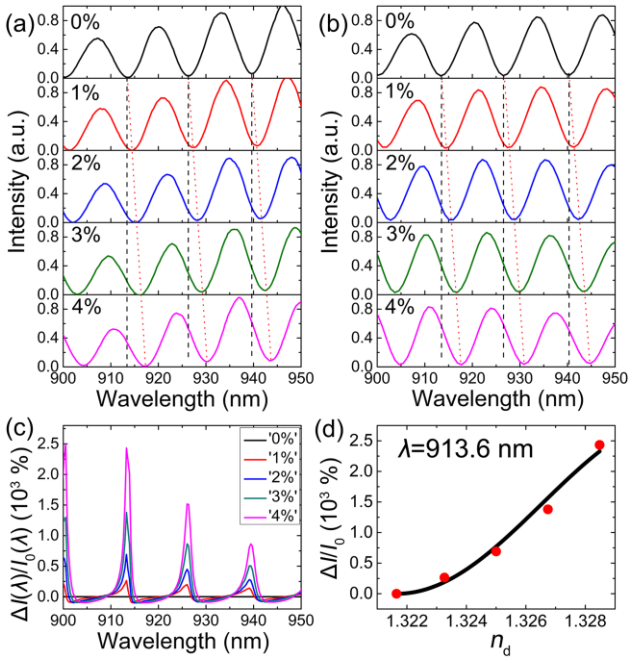

Fig. 3 (a) Experimental and (b) simulation results of the SPP interference spectra (wavelength ranged from 900 nm to 950 nm) in 0%, 1%, 2%, 3%, and 4% NaCl-H_2O solutions, respectively. The red dotted lines represent the wavelength position of the valley in different media, and the black dashed lines denote the destructive valley in water. (c) Experimental relative intensity changes ($\Delta I/I_0$) for different liquids. (d) Experimental results (red symbols) and theoretical fitting curve (black line) of the relative intensity changes ($\Delta I/I_0$) versus the refractive index.

Table 1. Experimental, simulation, and theoretical sensing performances for the double-slit structure at λ=925 nm.

Method	Sensitivity (nm/RIU)	Period (nm)	FOM (RIU^{-1})
Experiment	640	13.5	95
Simulation	655	13.6	96
Theory	692	14.3	97

Moreover, we can conclude from Fig. 3(a, c) that the relative intensity changes ($\Delta I/I_0$) increase with the contrast ratio of interference which agrees well with above theoretical analysis and Eq. (6). It is clearly observed from Fig. 3(c) that the maximum of the relative intensity change ($\Delta I/I_0$) is about 2500% at λ=900.2 nm and λ=913.6 nm. In Fig. 3(d), we plot the relative intensity changes ($\Delta I/I_0$) in the NaCl-H_2O solutions of different concentrations at λ=913.6 nm versus the corresponding refractive index, as shown by the red symbols. The black line is the theoretical curve by fitting $\Delta I/I_0$ data as a function of the refractive index with using equation of $\{1+C\cdot\cos[2\pi n_{eff}(n_d)L/\lambda]-I_0\}/I_0$ based on Eq. (1) and Eq. (2). The slope of the curve is the value of FOM* in Eq. (6).[30] It is observed that the experimental relative intensity changes ($\Delta I/I_0$) match well with the theoretical results. For the sensor, the maximal FOM* reaches about FOM*=4.7×10^3 RIU^{-1} around n_d=1.32700, where $\sin(\Phi)\approx 1$. This also accords well with Eq. (6). Such a high FOM* is more than 30 times that in the previous intensity-based single sensors,[24,30,35] where the values of FOM* are about 20 RIU^{-1} at 650 nm,[24] 120 RIU^{-1} at 590 nm,[30] 146 RIU^{-1} at 700 nm,[35] and 24 RIU^{-1} at 850 nm,[43] respectively.

Refractive index sensing in the double-slit aperture structure fabricated on the subwavelength plasmonic waveguide

Next, we investigate the sensing performance in a double-slit aperture structure which is fabricated on a subwavelength plasmonic waveguide,[44] as shown in Fig. 4(a). This subwavelength sensor is easily integrated on a chip. The inset in Fig. 4(a) is the sectional view of the plasmonic waveguide, which consists of a gold strip with a cross-section dimension of 300×100 nm^2 on a 350-nm-thick gold film. This subwavelength plasmonic waveguide supports a single SPP mode, as depicted in Fig. 4(b). The structure is fabricated by the FIB on a 450-nm-thick gold film. In the FIB fabrication process, the subwavelength plasmonic waveguide is fabricated by etching two 2-μm-wide grooves with a space of w between them on the gold film, leaving a subwavelength metal ridge on the metal surface to construct the plasmonic waveguide. Then, two identical rectangular apertures are fabricated in the plasmonic waveguide. The SEM image of the proposed sample is shown in Fig. 4(c), and its details are shown in Fig. 4(d, e). The measured structural parameters are about w_1=w_2=200 nm as before. Here, two samples with the slit spacing of L=19.69 μm and L=39.95 μm are fabricated in the experiment. On the left side of the double-slit structure with a separation of about 10 μm, a decoupling grating with a period of about 660 nm is also fabricated to scatter the SPPs, as shown in Fig. 4(d). Experiments

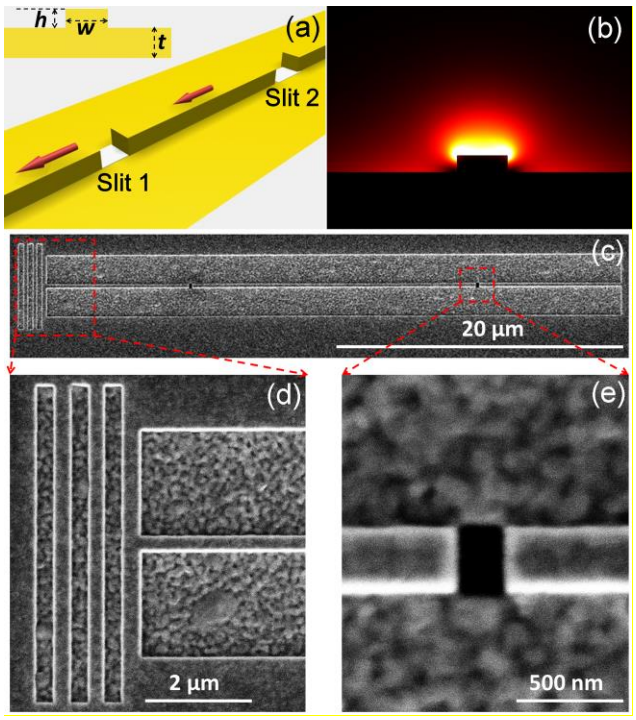

Fig. 4 (a) Schematic and geometrical parameters of the double-slit apertures on the subwavelength plasmonic waveguide. Inset shows the sectional view of the plasmonic waveguide with w=300 nm, h=100 nm, and t=350 nm. (b) Field distribution of the SPP mode supported by the subwavelength plasmonic waveguide. (c) SEM image of the experimental sample. (d) SEM detailed image of the scattering grating. (e) SEM detailed image of the double-slit aperture structure.

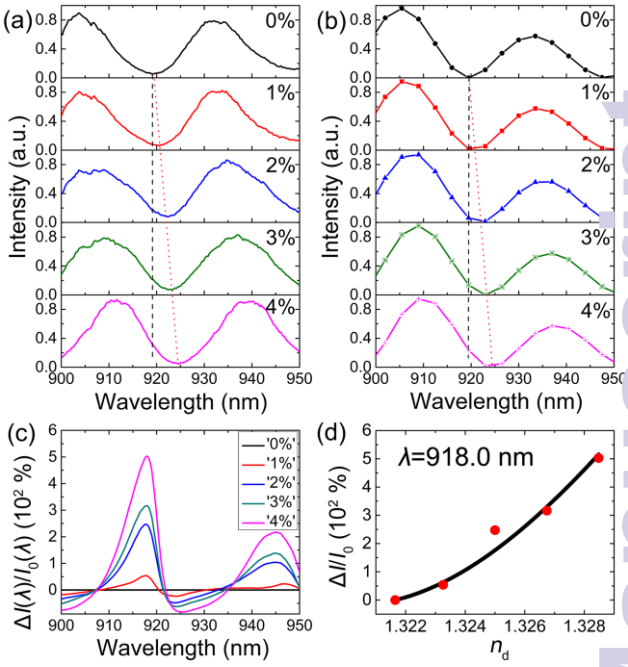

Fig. 5 (a) Experimental and (b) simulation results of the SPP interference spectra for the double-slit aperture structure in 0%, 1%, 2%, 3%, and 4% NaCl-H_2O solutions, respectively. Herein, the slit spacing is L=19.69 μm. The red dotted line represents the wavelength position of the valley in different media, and the black dashed line represents the destructive valley in water. (c) Experimental relative intensity changes ($\Delta I/I_0$) for different liquids. (d) Experimental results (red symbols) and theoretical fitting curve (black line) of the relative intensity changes ($\Delta I/I_0$) versus the refractive index.

show that the decoupling grating can be also fabricated on the subwavelength plasmonic waveguide.

When the p-polarized incident light impinges the two rectangular apertures from the back side, the excited SPPs will propagate along the subwavelength plasmonic waveguide until being scattered by the decoupling grating at the left side. To demonstrate the sensing process in such a double-slit structure fabricated on the plasmonic waveguide, we experimentally measure the interference spectra in 0%, 1%, 2%, 3%, and 4% NaCl-H_2O solutions. The measured results of the sample with the slit spacing of L=19.69 μm are shown in Fig. 5(a). Herein, the focused radius of the white light is about r≈15 μm, and the focused position is located at about 1-μm left of Slit 2. It is observed that the interference spectra exhibit oscillation behaviours with the period of about $\Delta\lambda$=29.5 nm, and they are red-shifted when the refractive index of the solutions increase. Correspondingly, the simulation data are shown in Fig. 5(b), which matches well with the experimental results. The sensing performances obtained from the experiment, simulation and theory are listed in the upper part of Table 2, and they are in good agreements, too. The relative intensity changes ($\Delta I/I_0$) as a function of the incident wavelength and the relative intensity changes ($\Delta I/I_0$) at λ=918.0 nm versus n_d are also calculated based on the measured results, as shown in Fig. 5(c, d). Due to the weak light [about 14% of that in Fig. 3(a)] scattered from the grating at the left side of the plasmonic waveguide, the values of the relative intensity changes ($\Delta I/I_0$) are obtained by smoothing the measured data. From Fig. 5(c, d), it is obtained that the maximum of relative intensity changes ($\Delta I/I_0$) is about 500,[illegible] and the maximal FOM* reaches about 1.2×10^3 RIU^{-1} when n_d=1.32848. In this case, we can get $\sin(\Phi)\approx0.87$, which is the maximal value of $\sin(\Phi)$ because of the large oscillation period ($\Delta\lambda$=29.5) and the small variation of refractive index (Δn_d=0.0068). Hence, this result also accords well with Eq. (6).

When the slit spacing is about L=39.95 μm, the focused radius of the white light becomes about r≈20 μm, and the focused position is located at about 2-μm left of Slit 2. The experimental and simulation results are shown in Fig. 6(a, b), and they agree well with each other, too. It is observed that the period of the interference spectra becomes smaller ($\Delta\lambda$≈15.0 nm). The sensing performances obtained from the experiment, simulation, and theory are listed in the lower part of Table 2, and they are also in good agreements. In the experiment, it is found that the signal intensities become only about [illegible]% of that in Fig. 3(a) because of the shorter propagation length (about 70% of that in the water-Au structure) and the quite small aperture (300×200 nm^2). This phenomenon can also be observed from the noise and burrs of the curves in Fig. 6(a). Due to the small signal and large noise, the contrast ratio is not a constant when changing the concentration of NaCl-H_2O solutions, as shown in Fig. 6(a). In addition, it can be seen from Fig. 6(c) that the maximum value of relative intensity change ($\Delta I/I_0$) is about 4400% at the incident wavelength of λ=948.3 nm, and we can get that FOM* of the single sensor reaches up to about 1.01×10^4 RIU^{-1} at λ=948.3 nm around n_d=1.32651, where $\sin(\Phi)\approx1$. This again matches well with Eq. (6).

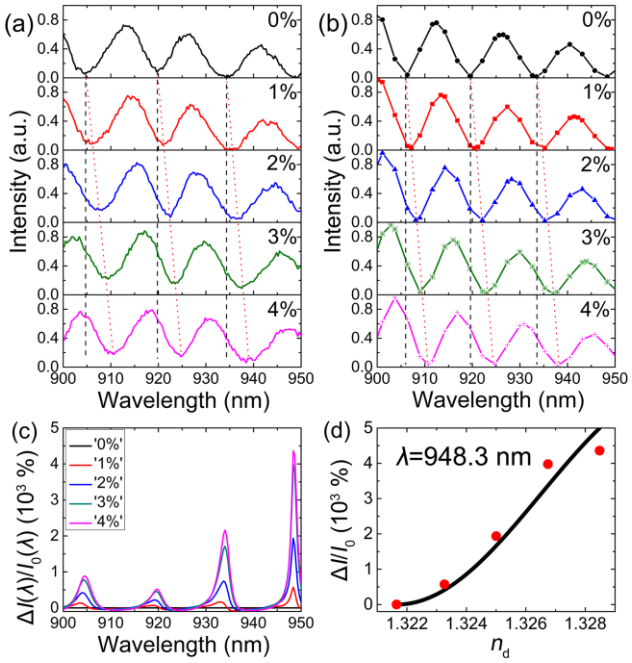

Fig. 6 (a) Experimental and (b) simulation results of the SPP interference spectra for the double-slit aperture structure in 0%, 1%, 2%, 3%, and 4% NaCl-H_2O solutions, respectively. Here, the slit spacing is L=39.95 μm. The red dotted lines represent the wavelength positions of the valley in different media, and the black dashed line represents the destructive valley in water. (c) Experimental relative intensity changes ($\Delta I/I_0$) for different liquids. (d) Experimental results (red symbols) and theoretical fitting curve (black line) of the relative intensity changes ($\Delta I/I_0$) versus the refractive index.

Table 2. Experimental, simulation, and theoretical sensing performances for the double-slit aperture structure fabricated on the subwavelength plasmonic waveguide with two different L at λ=920 nm.

L (μm)	Method	Sensitivity (nm/RIU)	Period (nm)	FOM (RIU^{-1})
19.69	Experiment	726	29.5	49
	Simulation	683	29.0	47
	Theory	684	31.5	43
39.95	Experiment	711	15.0	95
	Simulation	691	14.5	95
	Theory	684	15.5	88

Such a high FOM* is more than 70 times that in the previous intensity-based single sensors.[24,30,35,43] For the same conditions of the sensor (such as the laser fluctuation, environment noise, and detection resolution), the larger the FOM*, the higher the sensing resolution.[3,24,30,35] Therefore, the sensor of ultra-high sensitivities is experimentally realized by fabricating the double-slit aperture structure on the subwavelength plasmonic waveguide. This subwavelength sensor can be easily integrated on a chip, and it may find important applications in the sensing of particles and molecules.[45]

At last, let us compare the results of samples with the slit spacing of L=19.69 μm and L=39.95 μm. It is found that the refractive index sensitivity is independent of the slit spacing L, as predicted by Eq. (4). But the period of oscillation [$\Delta\lambda$ in Eq. (3)] is smaller when L becomes larger. Thus, a higher FOM can be obtained in the structure with a large slit spacing. Moreover, the large slit spacing L can give rise to a pronounced increase of FOM*, which can increase the sensing resolution significantly.[3,24,30,35] So the performance of structure with a larger slit spacing is better. But the propagation loss of SPPs also becomes larger for a larger slit spacing, which greatly increases the difficulty of balancing the two interference SPPs in the experiment as well as decreases the signal intensity. Thus, we should choose the modest spacing of the two slits due to the trade-off between the contrast ratio of interference and the slit spacing.

Conclusions

In summary, by fabricating a double-slit structure on a gold film of a subwavelength plasmonic waveguide, the high-contrast and broadband on-chip sensors were successfully demonstrated in the experiment based on the interference of SPPs excited from the two slits. By adjusting the focused position of the incident light on the double-slit structure to compensate the SPP propagation loss, a high contrast ratio of the interference was realized. By making use of the chromatism of the microscope objective, the different propagation loss was compensated in a broad bandwidth. As a result, a high-contrast ratio (≥0.9) of the interference spectrum in a broad band (>200 nm) was experimentally realized in the double-slit structure. Such a broad bandwidth made the double-slit structure robust to be designed and fabricated. Due to the high-contrast ratio, the intensity-based figure of merit (FOM*) could reach up to >1×10^4 RIU^{-1} (refractive index unit), which was more than 70 times that of the previous intensity-based single sensors.[24,30,35,43] The high-contrast, broadband, and high sensitive plasmonic sensor fabricated on the subwavelength plasmonic waveguide was easily integrated on a chip. Therefore, it might find important applications in the areas of environmental monitoring, biomedical research, and chemical research in highly integrated platform.

Acknowledgements

This work was supported by the National Basic Research Program of China (grant 2013CB328704) and the National Natural Science Foundation of China (grants 11204018, 61475005, and 11134001).

Notes and references

1. S. Lal, S. Link and N. J. Halas, *Nature Photonics*, 2007, **1**, 641-648.
2. X. Fan, I. M. White, S. I. Shopova, H. Zhu, J. D. Suter and Y. Sun, *Analytica chimica acta*, 2008, **620**, 8-26.
3. J. Homola, *Chemical reviews*, 2008, **108**, 462-493.
4. A. M. Armani, R. P. Kulkarni, S. E. Fraser, R. C. Flagan and K. J. Vahala, *Science*, 2007, **317**, 783-787.

5. C. A. Barrios, M. J. Banuls, V. Gonzalez-Pedro, K. B. Gylfason, B. Sanchez, A. Griol, A. Maquieira, H. Sohlstrom, M. Holgado and R. Casquel, *Opt. Lett.*, 2008, **33**, 708-710.
6. X. C. Yu, B. B. Li, P. Wang, L. Tong, X. F. Jiang, Y. Li, Q. Gong and Y. F. Xiao, *Advanced materials*, 2014, **26**, 7462-7467.
7. C. Rosman, J. Prasad, A. Neiser, A. Henkel, J. Edgar and C. Sonnichsen, *Nano letters*, 2013, **13**, 3243-3247.
8. P. Zijlstra, P. M. Paulo and M. Orrit, *Nature nanotechnology*, 2012, **7**, 379-382.
9. L. J. Sherry, S. H. Chang, G. C. Schatz, R. P. Van Duyne, B. J. Wiley and Y. Xia, *Nano letters*, 2005, **5**, 2034-2038.
10. W. J. Galush, S. A. Shelby, M. J. Mulvihill, A. Tao, P. Yang and J. T. Groves, *Nano letters*, 2009, **9**, 2077-2082.
11. C. L. Nehl, H. Liao and J. H. Hafner, *Nano letters*, 2006, **6**, 683-688.
12. T. Vo-Dinh, A. M. Fales, G. D. Griffin, C. G. Khoury, Y. Liu, H. Ngo, S. J. Norton, J. K. Register, H. N. Wang and H. Yuan, *Nanoscale*, 2013, **5**, 10127-10140.
13. G. K. Joshi, K. N. Blodgett, B. B. Muhoberac, M. A. Johnson, K. A. Smith and R. Sardar, *Nano letters*, 2014, **14**, 532-540.
14. N. Liu, M. L. Tang, M. Hentschel, H. Giessen and A. P. Alivisatos, *Nature materials*, 2011, **10**, 631-636.
15. W. Kubo and S. Fujikawa, *Nano letters*, 2011, **11**, 8-15.
16. N. Liu, T. Weiss, M. Mesch, L. Langguth, U. Eigenthaler, M. Hirscher, C. Sonnichsen and H. Giessen, *Nano letters*, 2010, **10**, 1103-1107.
17. A. V. Kabashin, P. Evans, S. Pastkovsky, W. Hendren, G. A. Wurtz, R. Atkinson, R. Pollard, V. A. Podolskiy and A. V. Zayats, *Nature materials*, 2009, **8**, 867-871.
18. V. G. Kravets, F. Schedin, R. Jalil, L. Britnell, R. V. Gorbachev, D. Ansell, B. Thackray, K. S. Novoselov, A. K. Geim, A. V. Kabashin and A. N. Grigorenko, *Nature materials*, 2013, **12**, 304-309.
19. K. M. Mayer and J. H. Hafner, *Chemical reviews*, 2011, **111**, 3828-3857.
20. Y. Shen, J. Zhou, T. Liu, Y. Tao, R. Jiang, M. Liu, G. Xiao, J. Zhu, Z. K. Zhou, X. Wang, C. Jin and J. Wang, *Nature communications*, 2013, **4**, 2381.
21. K. Matsubara, S. Kawata and S. Minami, *Appl. Opt.*, 1988, **27**, 1160-1163.
22. O. Telezhnikova and J. Homola, *Opt. Lett.*, 2006, **31**, 3339-3341.
23. Z. L. Cao, S. L. Wong, S. Y. Wu, H. P. Ho and H. C. Ong, *Applied Physics Letters*, 2014, **104**, 171116.
24. B. Zeng, Y. Gao and F. J. Bartoli, *Applied Physics Letters*, 2014, **105**, 161106.
25. A. Lesuffleur, H. Im, N. C. Lindquist and S.-H. Oh, *Applied Physics Letters*, 2007, **90**, 243110.
26. J. Homola, S. S. Yee and G. Gauglitz, *Sensors and Actuators B: Chemical*, 1999, **54**, 3-15.
27. Y. L. Chen and Q. Gong, *Physical Review A*, 2015, **91**, 013805.
28. Y. Gao, Q. Gan, Z. Xin, X. Cheng and F. J. Bartoli, *ACS Nano*, 2011, **5**, 9836-9844.
29. X. Wu, J. Zhang, J. Chen, C. Zhao and Q. Gong, *Opt. Lett.*, 2009, **34**, 392-394.
30. J. Feng, V. S. Siu, A. Roelke, V. Mehta, S. Y. Rhieu, G. T. Palmore and D. Pacifici, *Nano letters*, 2012, **12**, 602-609.
31. C. Wang, J. J. Chen, W. H. Tang and J. H. Xiao, *Chinese Physics Letters*, 2012, **29**, 127304.
32. Y. Gao, Z. Xin, Q. Gan, X. Cheng and F. J. Bartoli, *Opt. Express*, 2013, **21**, 5859-5871.
33. O. Yavas and C. Kocabas, *Opt. Lett.*, 2012, **37**, 3396-3398.
34. V. S. Siu, J. Feng, P. W. Flanigan, G. T. R. Palmore and D. Pacifici, *Nanophotonics*, 2014, **3**, 125-140.
35. Y. Gao, Z. Xin, B. Zeng, Q. Gan, X. Cheng and F. J. Bartoli, *Lab on a chip*, 2013, **13**, 4755-4764.
36. B. Zeng, Y. Gao and F. J. Bartoli, *Nanoscale*, 2013, **5**, 166-170.
37. X. Li, Q. Tan, B. Bai and G. Jin, *Opt. Express*, 2011, **19**, 20691-20703.
38. H. Raether, *Springer Tracts Mod. Phys.*, 1988, **111**, 1-133.
39. C. Ropers, C. C. Neacsu, T. Elsaesser, M. Albrecht, M. B. Raschke and C. Lienau, *Nano letters*, 2007, **7**, 2784-2788.
40. C. W. Sun, J. J. Chen, H. Y. Li and Q. H. Gong, *Opt Lett.*, 2015, **40**, 685-688.
41. D. K. Gramotnev and S. I. Bozhevolnyi, *Nature Photonics*, 2010, **4**, 83-91.
42. P. B. Johnson and R. W. Christy, *Physical Review B*, 1972, **6**, 4370-4379.
43. J. Becker, A. Trügler, A. Jakab, U. Hohenester and C. Sönnichsen, *Plasmonics*, 2010, **5**, 161-167.
44. J. Chen, C. Sun, H. Li and Q. Gong, *Nanoscale*, 2014, **6**, 13487-13493.
45. A. Ymeti, J. Greve, P. V. Lambeck, T. Wink, S. W. van Hövell, T. A. Beumer, R. R. Wijn, R. G. Heideman, V. Subramaniam and J. S. Kanger, *Nano letters*, 2007, **7**, 394-397.